JOURNAL OF MATERIALS SCIENCE **35** (2000) 1641–1659

The convergence-fault mechanism for low-angle boundary formation in single-crystal castings

R. E. NAPOLITANO*
Metallurgy Division, National Institute of Standards and Technology, Gaithersburg, MD, USA
R. J. SCHAEFER
Metallurgy Division, National Institute of Standards and Technology, Gaithersburg, MD, USA

A set of nickel-based superalloy single-crystal investment castings was evaluated for crystal perfection. Defect structures near the seed emergence point and other geometric features were examined using X-ray topography. Topographic images were compared with metallographically observed dendritic structures to establish a convergence-fault criterion for the location of low-angle boundaries. To support the phenomenological description of low-angle boundary formation through convergence-faulting, a tip-growth model for simulation of the growth of the dendritic network was developed. This model predicts the local primary growth direction from among three possible [001] directions and identifies regions of convergent growth. A connectivity parameter is defined and used to map the locations where convergence-fault formation is most likely. Predictions are compared with experimental observation.

1. Introduction

Continued advancement in the development of single-crystal gas-turbine engine components relies on achieving better control of the single-crystal casting process. As turbine blade geometries for advanced engines become more complex, process requirements become more stringent and production yield emerges as a limiting factor. Many types of performance-limiting crystal imperfections, such as freckles, spurious grains, recrystallized grains, and low-angle boundaries may be observed in a single-crystal casting. Given the cost constraints associated with design and development, casting designers must rely on simulation of the casting process to assess the potential yield for a given design. Such assessment requires techniques which can be used in conjunction with numerical thermal models for prediction of important microstructural features and defects. The development of these modeling strategies depends on an understanding of the forces and interactions which play important roles in the formation of various types of defects.

The mechanisms for formation of several types of grain defects are known in a general sense, and some progress has been achieved in quantifying them. For example, the formation of freckle channels by convective instabilities in the mushy zone has been modeled for multicomponent superalloys [1]. In this work, we are concerned with the formation of low-angle boundaries during solidification. In the past decade, these grain defects have been studied in some detail, but the mechanisms which account for their formation remain poorly understood. In 1989, Agapova *et al.* reported that the overall shape of the dendritic growth front, as dictated by the thermal gradient, is an important factor in the formation of low-angle boundaries [2]. In that study, a mosaic-like structure was associated with a dendritic front which is concave toward the liquid, and the relative misorientations were attributed to the situation where different parts of the front were advancing with different dendrite tip conditions. The effect of local solidification conditions was further pointed out by Paul *et al*. who measured very high liquid undercooling values in regions of a casting where the solid was forced to grow laterally across a platform [3]. The high local velocities and the rapid rate of latent heat release were concluded to be responsible for distortions in the crystal lattice, leading to a mosaic structure of subgrains. The effects of temperature gradient and isotherm velocity on single-crystal perfection were studied by Bellet *et al*. using gamma-ray diffractometry on cylindrical specimens grown from seeds [4]. Depending on the thermal constraint, boundaries between small groups of perfectly aligned dendrites were observed. The grouping of dendrites was attributed to lateral growth as the solid emerged from the seed. Siredey *et al.* observed similar structures at early stages of growth, where primary dendrites arrange themselves into rows along one or two of the secondary axes [5]. This alignment of primary stems into rows along the secondary directions was also observed by Rappaz and Blank, who attributed the structure to the growth of a series of tertiary branches originating from a single secondary arm [6]. Accordingly,

* *Present Address:* Ames Laboratory, Ames, IA, USA, E-mail: napolitano@ameslab.gov

these rows of dendrites initially form with a high degree of perfection which deteriorates significantly with growth [5, 7]. Degradation of the crystal as growth proceeds may be due to the rearrangement of the primary array, establishing regions of hexagonal and square arrangement, within regions of more random order, as observed by Siredey *et al*. [5].

In the first part of this investigation, we examine low-angle boundary formation in nickel-base alloy single-crystal castings with the objective of correlating their formation with the dendritic branching geometry, thus providing a means for defect prediction. The branching geometry itself, however, is not easily predicted, since it is influenced by the thermal conditions, the crystal orientation, and the mold geometry. In the second part of this study, we use a tip-growth model to simulate the growth of the dendritic structure through branch multiplication and extension within a given casting geometry. By employing a connectivity parameter for the dendritic network, self-convergence patterns are predicted, indicating likely locations for low-angle boundary formation.

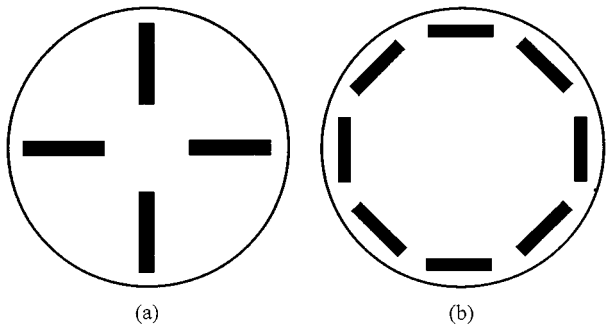

Figure 1 The layouts of the (a) radial and (b) tangential casting clusters within the cylindrical directional solidification furnace.

2. Experimental

Two sets of test castings, made from nickel-based alloy Rene N5 using standard single-crystal investment casting production procedures were used for this investigation. One set was a radially arranged cluster of four castings while the other was a tangentially arranged cluster of eight castings, as shown in Fig. 1. One casting from each group was used for this study, and the geometry and dimensions of each are described in Fig. 2. The radially oriented casting, designated specimen R, was a simple slab shape with a rectangular cross-section and a 45-degree expansion zone. The tangentially oriented casting, specimen T, also had a rectangular cross section, however it had an expansion zone with a 30° incline on one side and a 45° incline on the other. Additionally, the tangential casting design included a platform, which was placed at a 10° angle on the side where the expansion zone angle was 30° and a 20° angle on the side where the expansion zone angle was 45°. This platform extended 6 mm beyond the front and back faces of the casting and approximately 25 mm beyond the side faces of the casting. For both castings, a seed crystal was used which was oriented such that the primary dendrite axis and one secondary axis would lie within the plane of the largest flat surface.

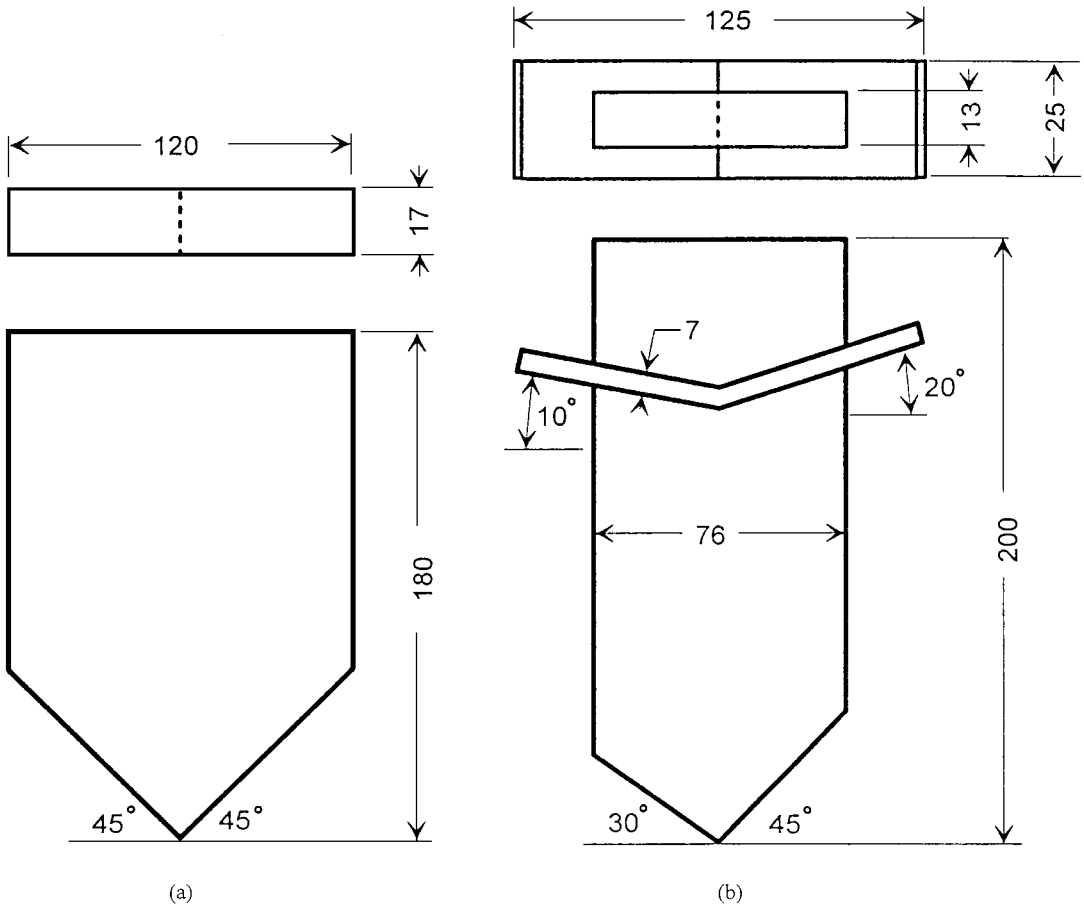

Figure 2 The geometry of (a) the radial casting and (b) the tangential casting. The dimensions given are in millimeters.

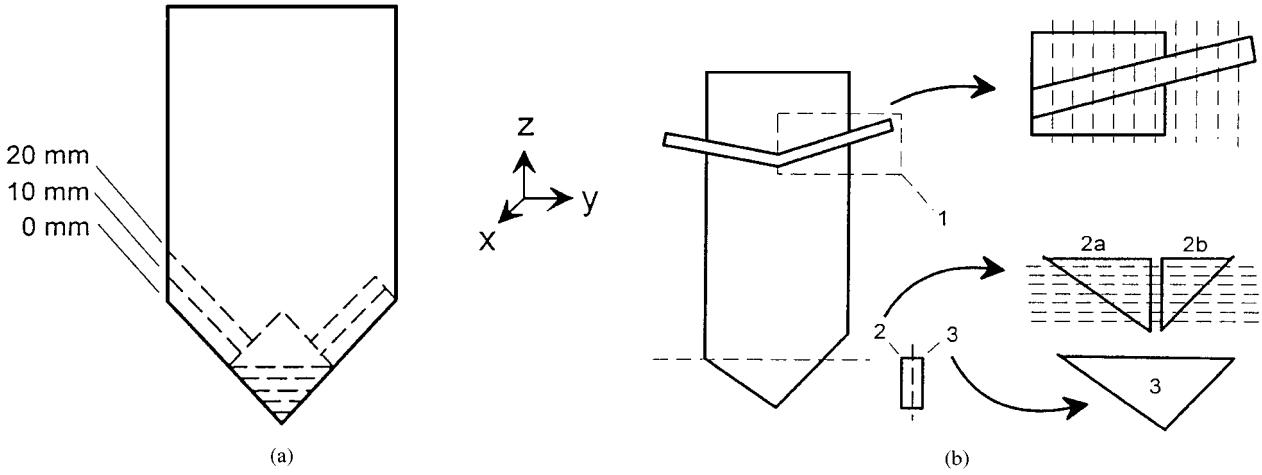

Figure 3 The sectioning plans for (a) the radial and (b) the tangential castings.

The specimens were etched to reveal the dendritic structure at the surface and examined optically, at magnifications up to 40×. Because of the crystal orientation, primary dendrite directions were easily distinguishable on the casting surface, permitting visual measurement of grain orientations. To further reveal their dendritic structures, specimens R and T were sectioned for metallographic analysis, as shown in Fig. 3. Specimen T was sectioned through the midplane and then transversely with a series of cuts, 3 mm apart, from the seed emergence point through the expansion zone. This type of serial sectioning was also performed for the platform region of specimen T. Specimen R was serially sectioned through approximately one third of the expansion zone. It was then sectioned parallel to the sloping walls of this region. Samples were mounted and polished to 0.05 μm, etched, and examined metallographically.

X-ray topographic analysis was performed on selected metallographic specimens to evaluate the degree of perfection in the dendritic structure. This method involves irradiating an area of the specimen with monochromatic parallel X-rays and positioning the film, or other imaging detector, in a location consistent with a particular diffraction condition. An image of all regions of the specimen, which satisfy the prescribed diffraction condition, is produced. All topographs shown here were obtained using the 200 reflection. Using this technique, various grain defects can be identified and their position can be compared with mold geometry, seed location, and the branching patterns which comprise the dendritic structure. The topographic analysis was performed using 8 keV synchrotron radiation monochromated with an asymmetrically cut Si {111} double-crystal. Topographs were recorded on high contrast film as well as video tape.

3. Results

3.1. Visual surface examination and optical metallography

Several types of grain defects were readily visible on the etched surfaces of the castings, including freckle chains, low angle boundaries, and spurious grains. The surface of specimen T is shown in Fig. 4. Freckles are numerous on the outward facing side (side-A) of specimen T, but none are visible on the inward facing side (side-B). The freckles observed on side-A initiated along a horizontal line near the top of the expansion zone and propagated outward as they moved upward. This line also delineates an apparent change in the geometry of the dendritic network. Below this line, primary dendrites dominate the structure, and secondary arms were not observed to extend beyond the adjacent primary dendrites. Beyond this location, however, some significant secondary growth was observed, indicating adjustments in primary spacing and dendritic array geometry.

Visual measurements of primary dendrite orientation at the casting surface, indicate misorientations less than 10° in regions below the platform but much higher in regions above the platform. A map of the measured orientations is shown in Fig. 5. The highly misoriented regions above the platform are due to spurious grains, which may have nucleated in the platform region or may have grown from dendrite fragments, which have been transported to this region through convective flow. In any event, we will not consider these defects further since we are presently concerned with low-angle boundary formation. In the lower portion of the casting, nearly all observed low-angle boundaries could be visually traced all the way down to a mold wall or a freckle grain. Several individual freckle grains are visible within each of the freckle channels. In some locations, it is apparent that a low-angle boundary was formed when a freckle grain was permitted to grow for an appreciable distance before being extinguished by the more favorably oriented primary crystal. These observations suggest that the freckle grain came to rest near the primary front with an orientation very close to that of the primary grain. In such cases, the freckle grain may compete with the primary front, resulting in a low-angle boundary. Freckle grains which come to rest in a channel well behind the primary front and those which are not oriented near the primary crystal orientation, however, cannot compete and are quickly extinguished. High-angle boundaries may also be produced if the freckle grain is ejected from the channel

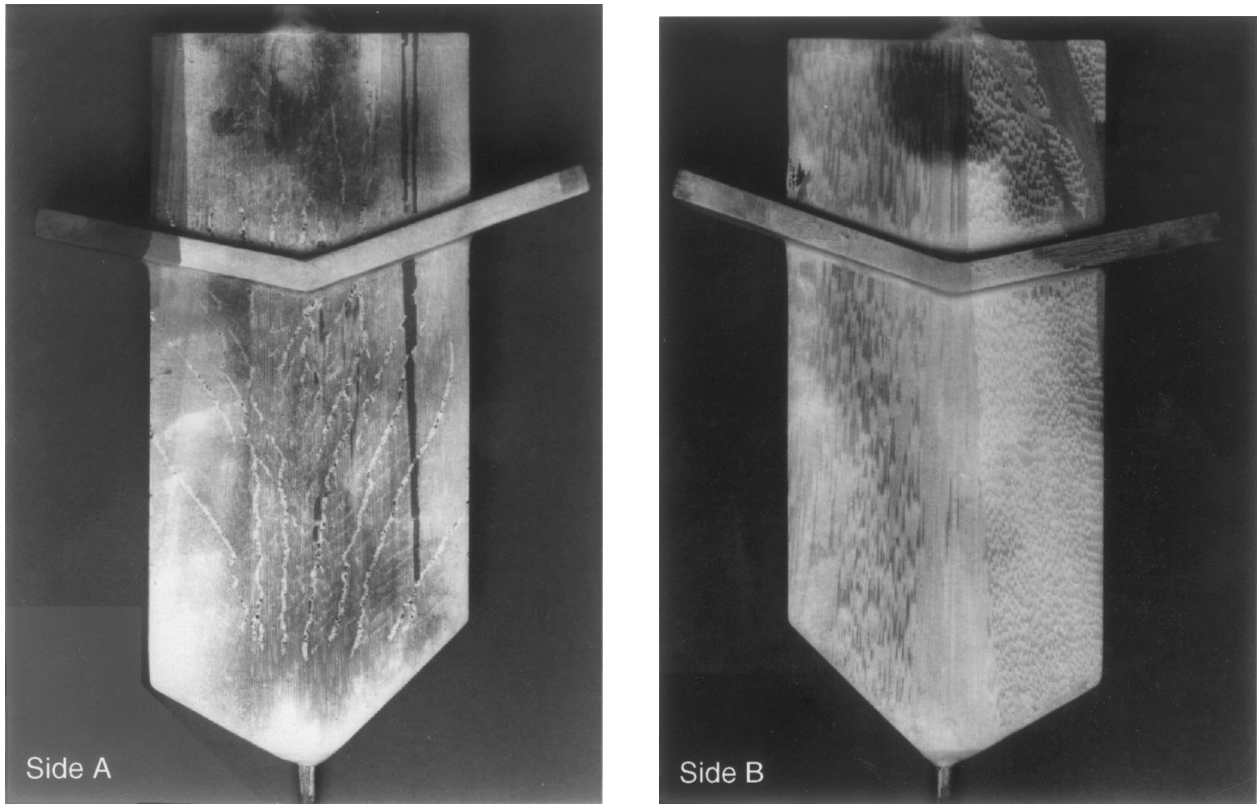

Figure 4 The surfaces of the tangential casting after etching to reveal the dendritic structure. Grain defects such as freckle chains, low-angle boundaries, and spurious grains are visible.

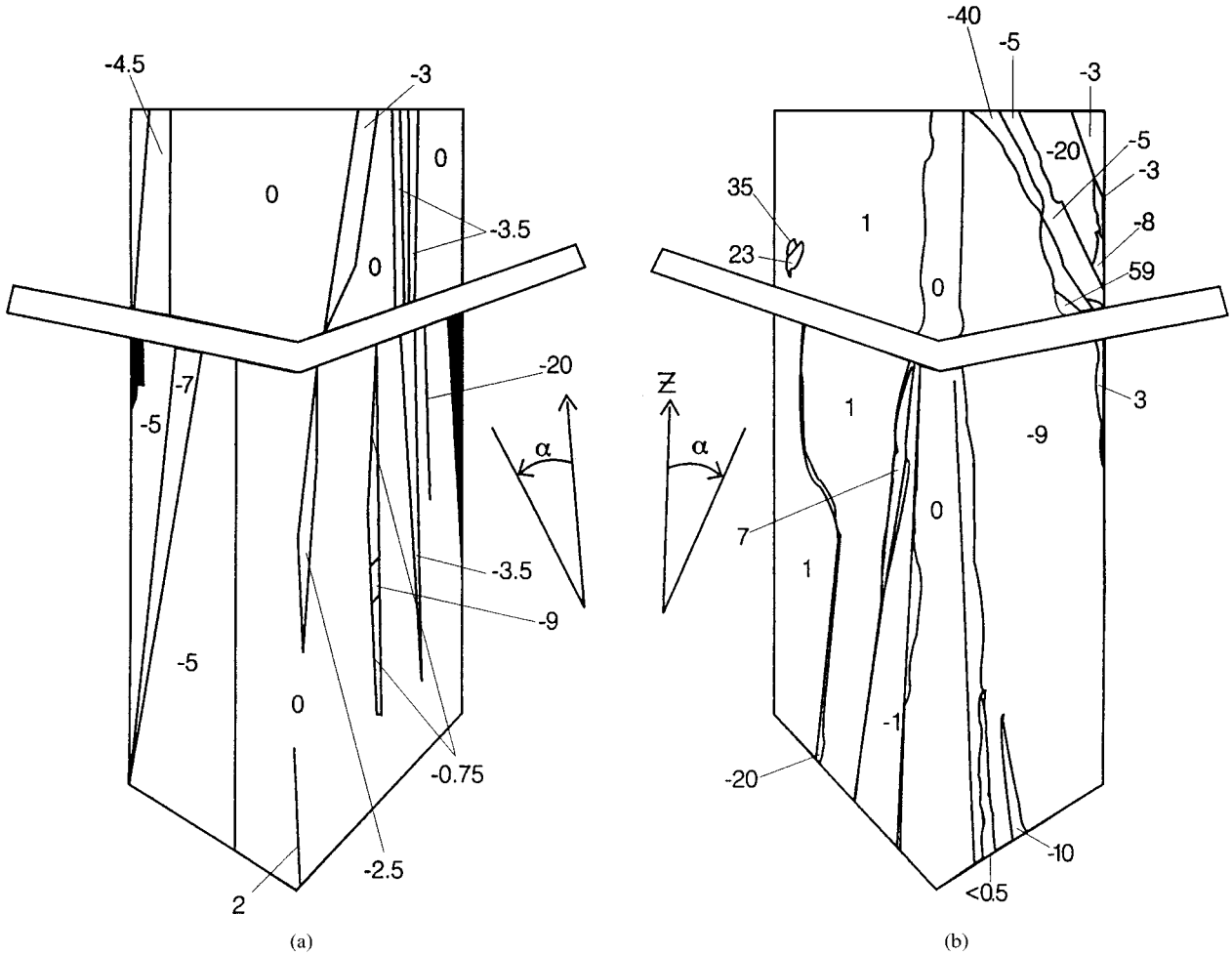

Figure 5 The orientation of the primary dendrites, as measured on the surface of specimen T. The angular values given indicate the primary direction projected onto the plane of the casting surface. (a) Outward facing side, (b) inward facing side.

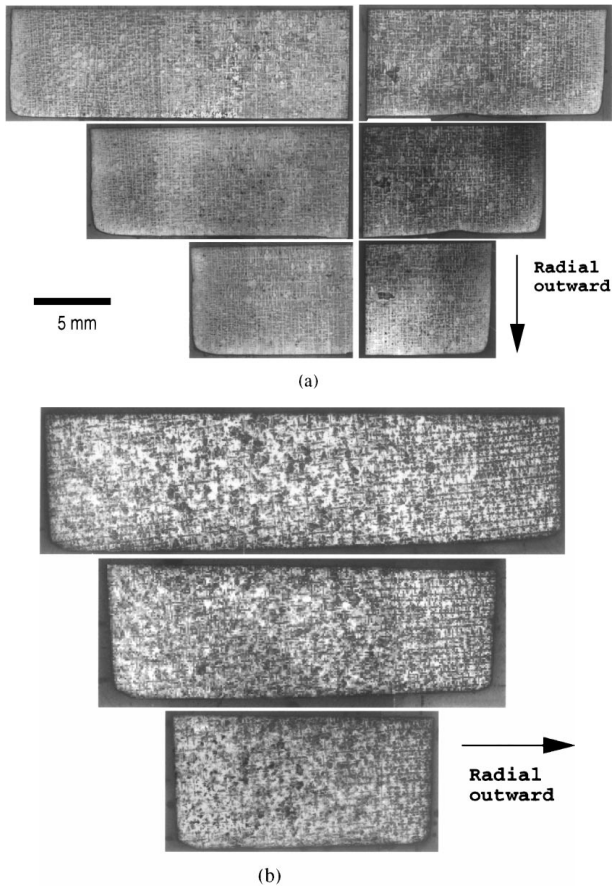

Figure 6 A series of parallel transverse views of the microstructure for (a) the tangential and (b) the radial casting. For each series, the views shown are for sections which are 5, 10, and 15 mm from the seed emergence point, progressing from bottom to top. For each view, the upper border is a section plane while the other three borders indicate the casting surface.

into the bulk liquid and the thermal/solutal conditions permit growth of the randomly oriented grain [8]. In any case, whenever freckles are present, they must be considered as potential sources of low and, in some cases, high angle boundaries. Of the boundaries which extend down to the mold wall, only one was observed to initiate near a mold surface anomaly. Defects in the mold wall itself, therefore, were ruled out as the primary cause of boundary formation. The mold geometry, however, may influence boundary formation by locally constraining growth of the solid, resulting in complex growth patterns in the primary array and a wide range of tip conditions over the entire dendritic envelope. These patterns may result in a self-convergent growth front, particularly in areas of nonuniform cross section, such as the expansion zone, making boundary formation likely in these locations.

Our evaluation of the effect of the mold geometry on the dendritic structure begins with the determination of the local primary growth direction. Near the mold wall in the expansion zone, the dominant dendrite growth direction was observed to be different for the two castings. For specimen R, the primary dendrites were observed to grow in a stair-step fashion straight up the sloping surface of the mold wall, with only very short secondary branches in the x-direction. This indicates that the dominant secondary direction is along the

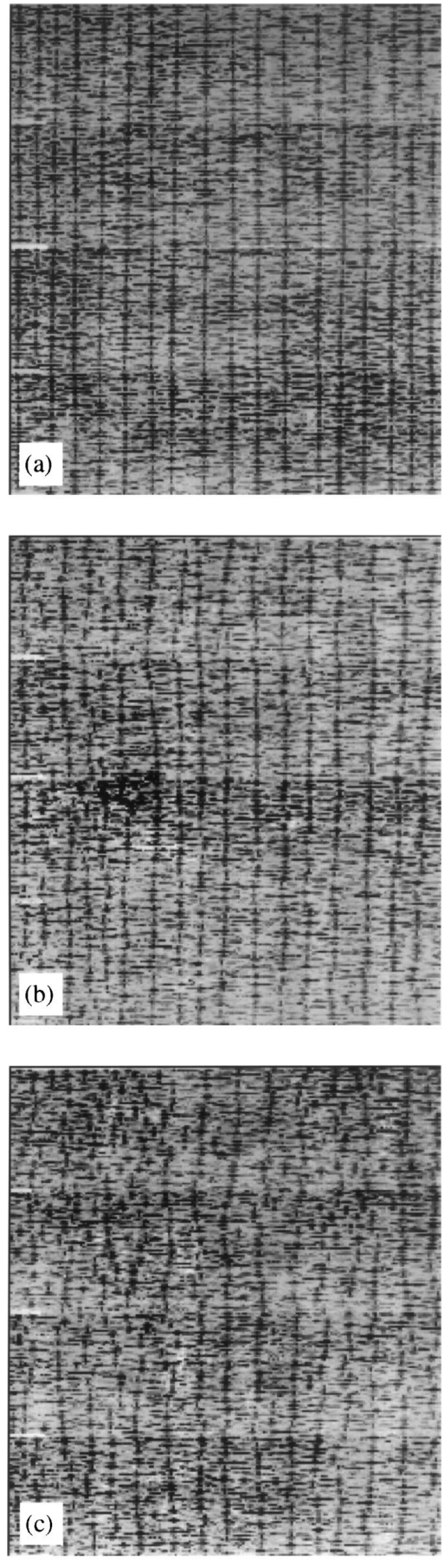

Figure 7 The dendritic structure in casting R as viewed on a plane parallel to the mold wall in the expansion zone. The images have been compressed vertically to reveal the dendrite alignment, with the dendrite cores in dark contrast. Each image includes an area of 7 mm on the horizontal axis by 40 mm on the vertical axis. Distance from section plane to mold wall: (a) 0 mm, (b) 10 mm, (c) 20 mm.

y-axis. For specimen T, however, examination of the sloping surface of the mold wall showed that growth had progressed in stair-step fashion along the outside corners, and secondaries then spread along the *x*-axis, through the thickness of the casting from side-A to side-B, toward the center of the furnace. As a consequence of these differences, the general alignment of the dendrites seen in transverse sections of specimens T and R was different, as illustrated in Fig. 6. In both castings, the primary growth direction is normal to the image, but the dendrites are ordered into rows within the plane of the section. These rows are oriented along the *y* direction for specimen R but along the *x* direction for specimen T. In both cases, the primary dendrites are aligned into rows along the radial direction of the furnace, regardless of the casting geometry, as a result of their origin from the dendrites which spread across the sloping surface in the expansion zone. Fig. 6 also indicates that the degree of ordering among the primary dendrites is very high near the mold wall but that it deteriorates rapidly as the front grows away from the wall. This property is also illustrated in Fig. 7, which shows the microstructure on a series of sections taken parallel to the mold wall of specimen R. The wall is oriented at 45° to the primary direction. Thus, these figures actually show a series of branching corners which formed as the dendritic solid propagated up the wall in a stair-step fashion. The images in this figure have been

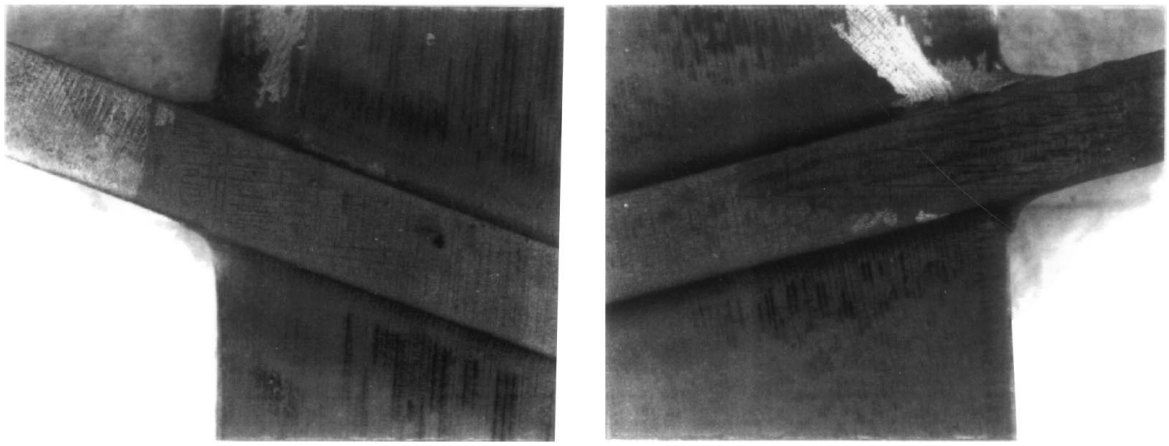

Figure 8 Laterally oriented dendrites, growing from the outer edge of casting T, toward the centerline, were observed on the outer surface of the side-B platform. On side-A, only vertically growing dendrites were observed.

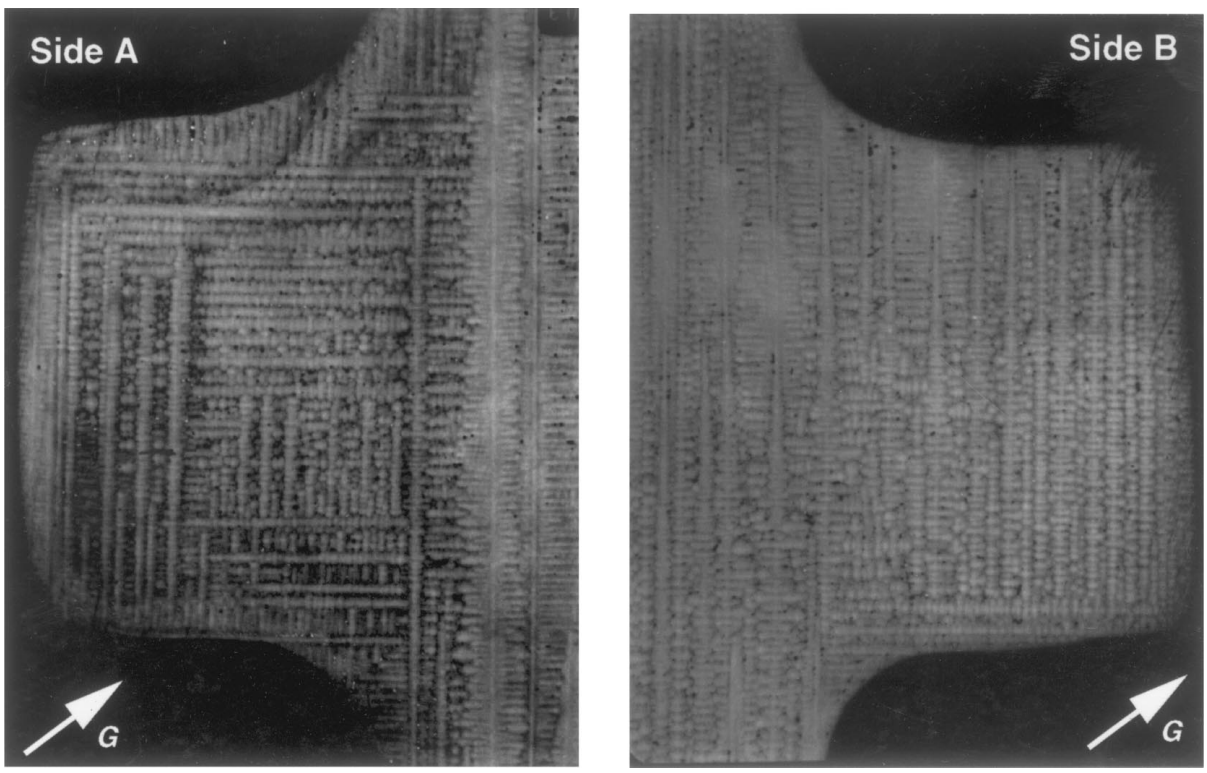

Figure 9 The difference between the dendritic structures within the two sides of the platform on specimen T illustrates the influence of geometric constraint on the conditions at the advancing front. On side-A, a complex branching pattern is generated due to the high undercooling that develops as a result of the constraint of the mold corner. On side-B, the temperature gradient points outward, allowing the front shape to follow the isotherm shape, minimizing the undercooling. The resulting dendritic structure is well ordered and dominated by growth in the primary direction.

compressed in the vertical direction to more clearly illustrate the deterioration of layer perfection. At the mold wall, virtually every layer extends through the entire length of the figure without interruption. At 10 mm, layers extend for significant distances but jogs are visible in most. At a distance of 20 mm from the mold wall, perfection of the dendritic array is very poor, particularly in several localized regions where no evidence of layering remains. The observations in the expansion zone indicate that when the dendrites first grow upward from the sloping mold surface, they are geometrically well-aligned into rows as a result of their origin from secondary branches which grow in the radial direction of the furnace. However, the farther the dendrites grow upward from the sloping mold walls, the more the alignment into rows deteriorates. This loss of alignment is not in itself a defect, but it suggests crystallographic variation within the dendrites, which would form the basis for an accumulation of primary direction change which can lead to low-angle boundary formation.

We now turn our attention to the platform region in specimen T. The surface dendrites provide clear evidence that the geometry of the platform had very different effects on the two sides of the casting. On side-B, many dendrites were observed growing laterally inward on the surface of the platform near the side faces of the castings, as shown in Fig. 8. These were not observed on side-A. Analysis of the internal dendritic structure in the platform region reveals further differences between the two sides of the casting. The structures observed on each side of the platform, as viewed on an x-z plane approximately halfway from the centerline to the casting edge, beyond the region of lateral growth, are shown in Fig. 9. On side-A, the dendrites branch out into the platform, up along the front face, and back toward the casting midplane where they converge with secondary branches growing in the opposite direction. On side-B, the entire platform is characterized by primary dendrites growing along the z direction in a coordinated fashion.

3.2. X-ray topography

Topographs from sections taken parallel to the sloped surface of the expansion zone of specimen R, at distances of 0 and 20 mm from the mold wall are shown in Fig. 10. These indicate that the crystallographic perfection of the casting is highest near the mold wall in the expansion zone and that it decreases rapidly with distance from this surface. Along the wall, continuous structures, representing single dendrites which propagate up the mold wall by successive branching, are visible and remain in contrast over long distances, as shown in Fig. 10a. These correspond to the well ordered rows of primary dendrites shown in Fig. 7a. At a distance of 20 mm from the mold wall, Fig. 10b, no such

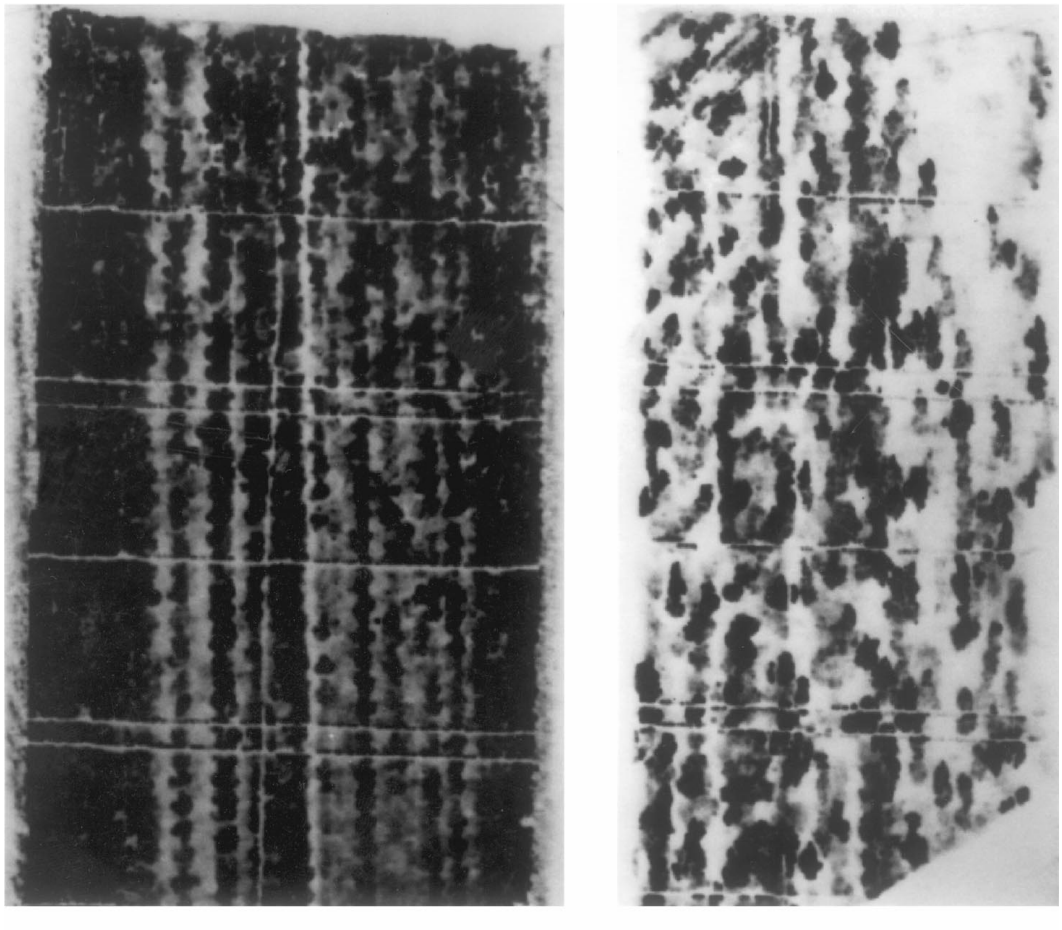

(a) (b)

Figure 10 X-ray topographs of the sections shown in Fig. 7, taken parallel to the mold wall in the expansion zone of casting R. (a) Along mold surface, (b) 20 mm from wall. The thin white lines were intentionally scribed for reference purposes.

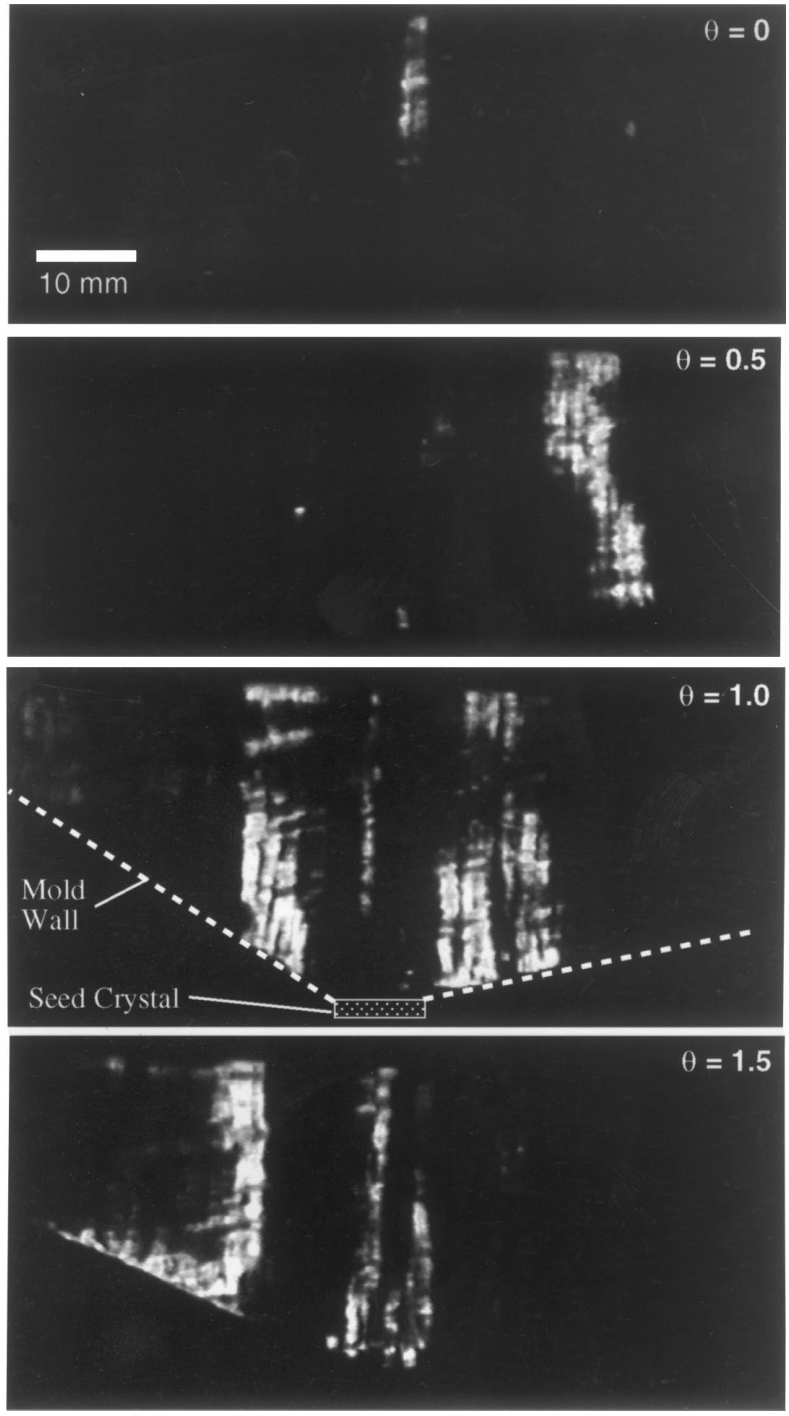

Figure 11 X-ray topography within the expansion zone from the midplane of specimen T reveals several well defined defect features, or regions of similar orientation divided by low-angle boundaries. The angles given are relative tilt values about the horizontal (y) axis. The dimensions are approximate due to minor distortion which results from misorientation about axes other that this tilt axis.

structures are observed. Diffracting features are small and more randomly positioned than those along the surface, demonstrating that the deterioration of geometric alignment of dendrites, seen in Fig. 7c, was accompanied by a deterioration of crystallographic alignment.

Topographs from the midplane of the expansion zone of specimen T indicate the presence of well defined defect structures which are made up of small packets of dendrites, as shown in the series of topographs in Fig. 11. These structures were observed to extend from the expansion zone surface through the entire length of the expansion zone, and may continue much further. Topography of the serial transverse sections also reveals the presence of these structures. Fig. 12 shows several defect structures observed on a transverse plane approximately 5 mm into the expansion zone, in specimen T. To illustrate the persistence of these defect structures, the topographic images of a single feature, as observed on the first five transverse sections in the expansion zone, are shown in Fig. 13. The relative variation of misorientation along the growth direction between each of the defect structures, shown in Fig. 12, is plotted in Fig. 14. This figure shows that the relative misorientation between the defect structures remains constant, suggesting that, once the boundary is formed, there is no further orientation variation. This is consistent with

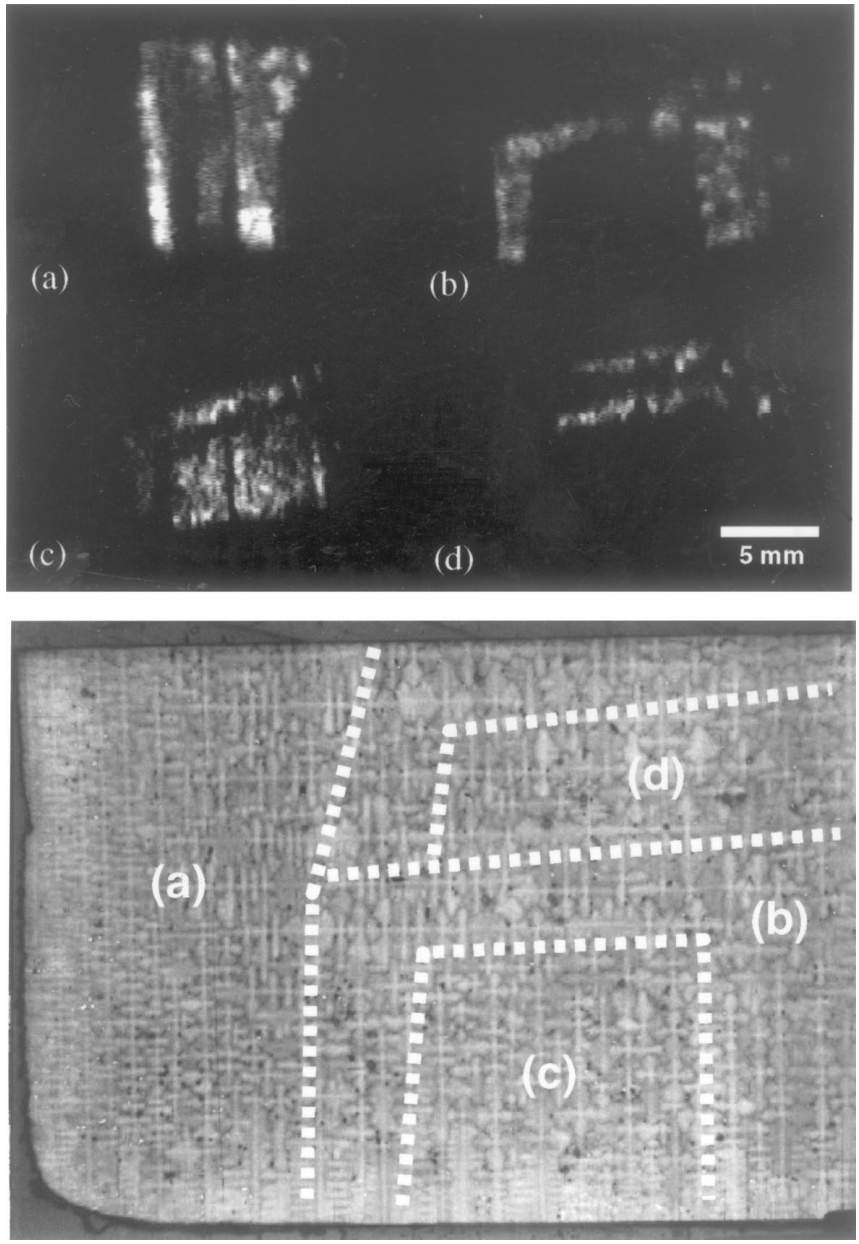

Figure 12 Topography of a transverse section reveals several defect features which have formed in very early stages of growth, within 5 mm of the seed emergence point. The approximate location of each feature on the sectioning plane is indicated. The structure shown is from the lower left image in Fig. 6a. The different features were brought into contrast by tilting the specimen about the vertical (x) axis.

the fact that only those low-angle boundaries observed on the first serial section are observed throughout the expansion zone. These observations indicate that no distinct boundaries were formed away from the mold wall, even though the dendritic array was evolving and the overall crystal perfection was observed to be deteriorating.

X-ray topographs from the serial sections in the platform region of specimen T also reveal the presence of defect structures which propagate for long distances in the z direction. Additionally, like the metallographic investigation of the platform region, topographic analysis revealed significant differences between side-A and side-B of specimen T. Two series of topographs, taken from the section shown in Fig. 9, are shown in Fig. 15. The platform on side-A is clearly at a different orientation from the bulk casting. The entire platform is separated by a vertical boundary, but there is little substructure within the platform itself. Side-B does not exhibit such a boundary between the platform and the bulk. Instead, there are some internal structures, including an L-shaped boundary at the lower portion of the platform.

4. Discussion of results

The primary type of defect observed in the expansion zone is the low angle boundary, where, during the process of branching and spreading, the dendritic grain has become locally misoriented. The mechanisms which may lead to the development of such misorientation in a dendritic grain are not well understood, yet we can consider misorientation to evolve in one of two ways. A dendrite could experience a change in orientation as a direct response to some applied force to the primary stalk, which could be thermal (dendrite not aligned with

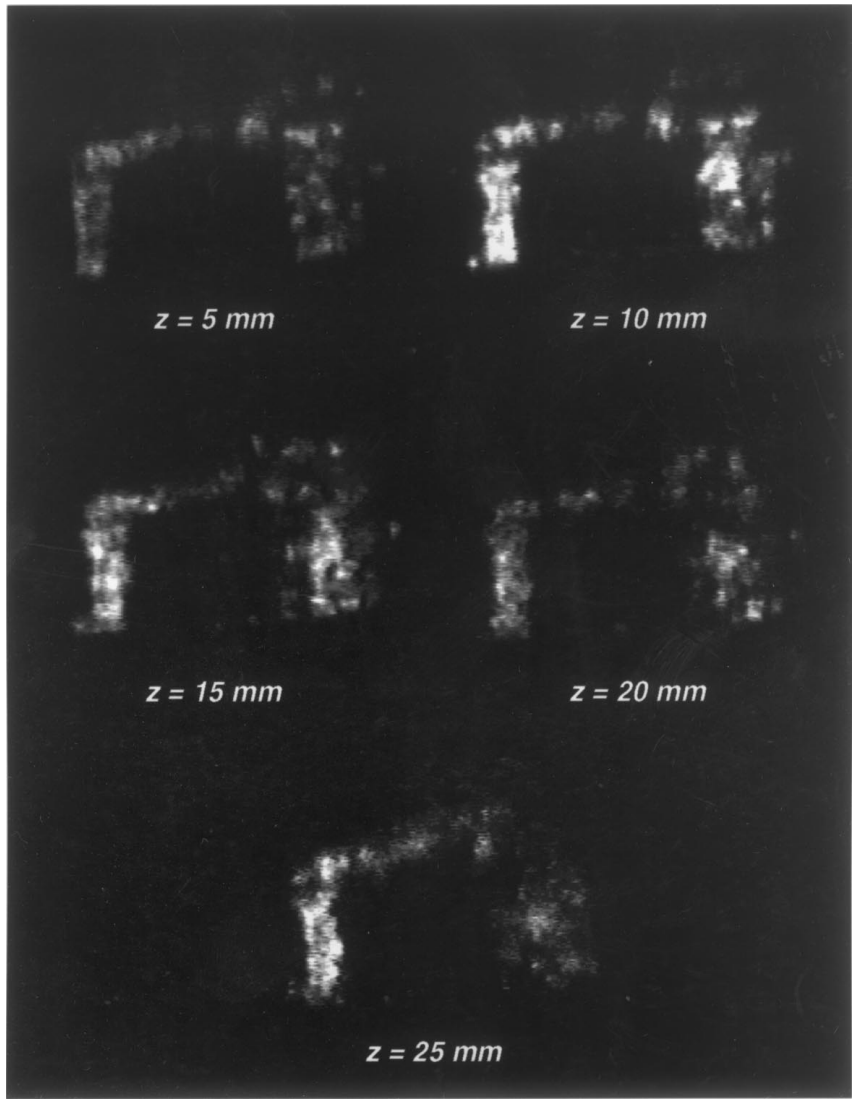

Figure 13 Several grain defects were observed to persist throughout the expansion zone, as shown above for the structure pictured in Fig. 12b. The orientation and definition of various features, however, vary with growth distance. The *z* value given is the distance from the seed to the section plane.

local gradient), chemical (asymmetric solute field), or mechanical (fluid flow). Alternatively, orientation shifts could result from a process where the most favorable growth conditions are selected from a multitude of perturbed orientation states. The existence of such perturbations is suggested by the optical and topographic observations of specimen R (Fig. 10), which show that it is possible for dendrites which are initially growing with very good geometric and crystallographic alignment to gradually and unsystematically become less well aligned. The development of a distinct boundary, however, requires some mechanism for the accumulation of these local orientation variations into clearly distinguishable regions of differing orientation. Whether a local orientation adjustment is the result of an applied force or of the selection from a number of perturbed states, however, it is probable that such an adjustment would be different for dendrites propagating in spatially separated or disjointed parts of the casting, where the applied forces or selecting factors are different. If the geometry of the casting permits these disjointed growth front segments to rejoin, the dissimilar orientations of the two segments may result in a low-angle boundary along the surface of impingement. Because this mechanism of boundary formation involves convergence of two parts of the growing crystal, we refer to this type of boundary as a convergence-fault. Regardless of the mechanism which triggers the orientation shift, it is clear that disjointed grains will be prone to the formation of these convergence-faults. These defects can be formed on a large scale, with dimensions on the order of the casting size, or on a very fine scale, where the disjointed regions include only a few dendrites. Whatever the mechanisms responsible for dendrite misorientation, they will tend to produce low-angle boundaries along convergence-faults.

We will now examine the formation of convergence-faults from the standpoint of interactions between dendritic branching patterns, mold geometry, and thermal conditions. Early in the solidification process, as the front moves through the expansion zone, the mold geometry and orientation in the furnace have a significant effect on the ordering of the primary dendritic array, and the primaries tend to arrange themselves into rows along the dominant secondary direction, which is the secondary direction of highest growth rate. The hierarchical formation of these structures is affected by the constraints of the mold geometry, resulting in the

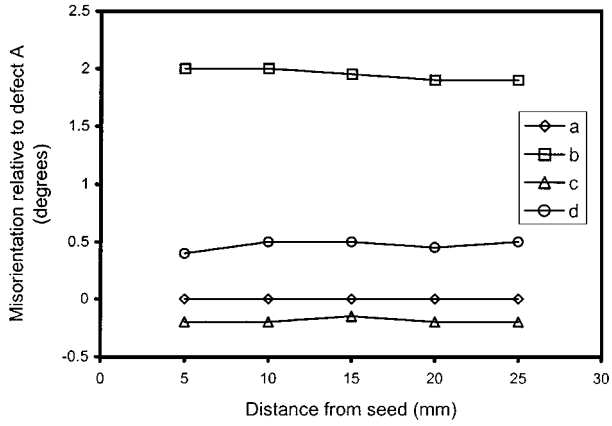

Figure 14 A plot of the relative angular variation through the expansion zone for the defect structures shown in Fig. 12. Labels a through d refer to features shown in Fig. 12. Feature a was used as a reference.

defect structures observed topographically. Evidence of this convergence-fault mechanism can be seen in Fig. 12. The section shown is a one-quarter cross section through the expansion zone of specimen T, where the top edge of the section is the casting midplane, the right edge is the casting centerline, the left edge is the surface of the expansion ramp and the bottom edge is the outboard face. The sectioning plane shown is approximately 5 mm above the seed, which is located immediately beneath the upper right corner of the section. Recall that the dominant secondary direction is through the thickness, from side-A toward side-B which is bottom to top in this figure. Because the seed is located at the midplane, however, the through thickness growth cannot occur at all locations. When the front emerges from the seed, side-A is cooler than side-B, and the solid spreads along the side-A face and begins to propagate through the thickness of the casting. While the solid spreads across this face, however, growth proceeds in other directions from the seed, as well. The impingement planes, which divide regions of differing dendrite ordering, are indicated by discontinuities in the observed branching geometry and may be associated with convergence-faults. Because the dendrites involved in the emergence from the seed are relatively few, the regions formed by the resulting growth patterns may be very small yet complex in shape.

The interactions between the thermal field, the mold geometry, and the dendritic branching geometry are also evident in the defect structures which form in the platform region of the casting (see Figs 8, 9 and 15). To understand these interactions, shown schematically in Fig. 16, we first make some generalizations regarding the shape of the liquidus isotherm as it moves through the tangential casting. Because freckle channels tend to migrate toward the highest points of the interface [9] and the freckles observed in specimen T all migrated toward side-A, we conclude that the through-thickness thermal gradient is from side-A to side-B. Furthermore, the freckles that migrated outward toward the side faces indicate that the isotherms are concave upward, as illustrated in Fig. 16a. As this type of front interacts with the platform geometry, there are two geometric features of the mold to consider. The cross sectional change in the

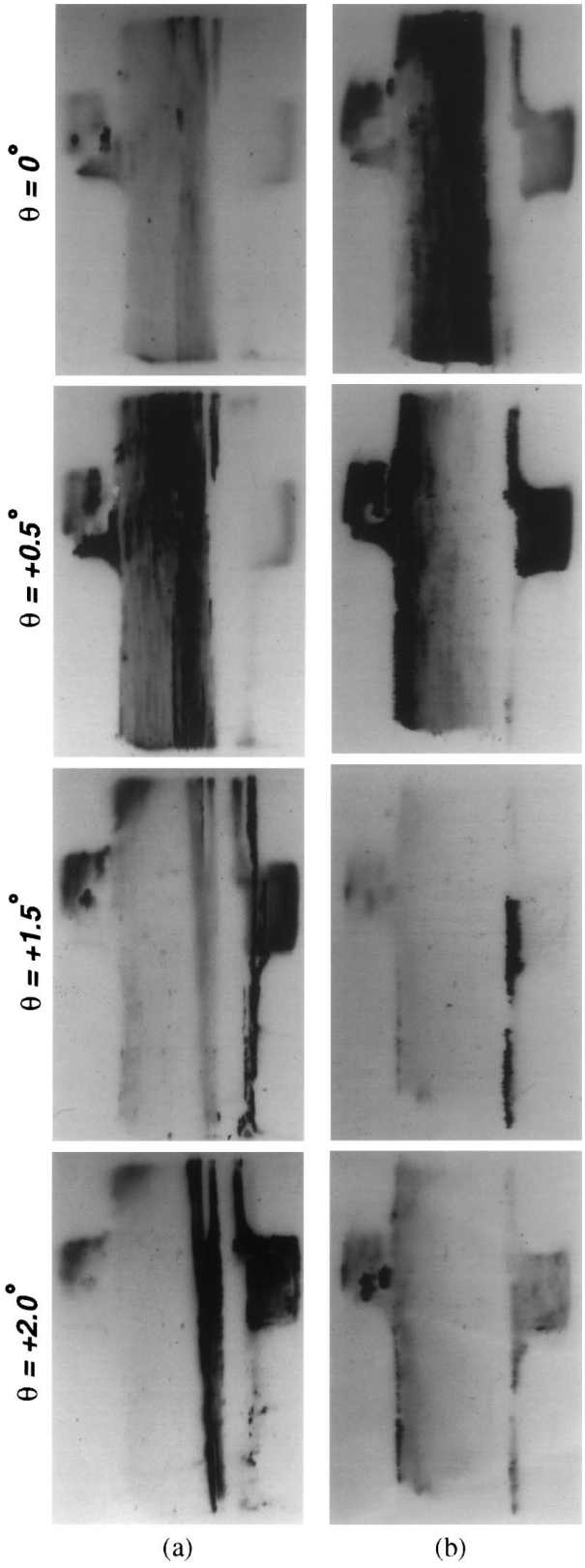

Figure 15 X-ray topographs from a section plane near that shown in Fig. 9. The angles given indicate relative tilt about (a) the horizontal (x) axis or (b) the vertical axis (z). For each view, side-A is on the right and side-B is on the left.

x-z plane is shown in Fig. 16b along with the geometry of the moving solidification front. Clearly, the conditions on the outboard side differ greatly from those on the inboard side of the casting. As the front approaches the platform, $t = t_1$, a significant degree of undercooling develops in the liquid within the platform on the

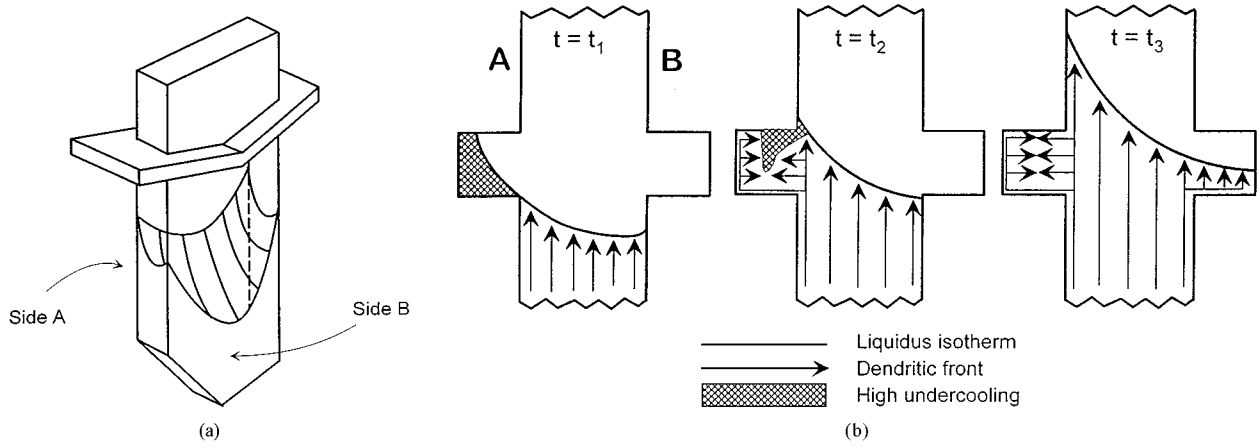

Figure 16 (a)The general shape of the isotherms as estimated from the microstructure of the casting, (b) A schematic representation of growth into the platform region, illustrating the difference in the dendritic patterns due to the effect of the platform geometry and the through-thickness gradient.

outboard side. The shape of the mold, however, prevents growth into that region. As the front passes the mold corner, $t = t_2$, lateral growth into the platform is very fast due to the high undercooling. In a fashion similar to that observed in the expansion zone, an irregular dendritic pattern, like that shown in Fig. 9a, is developed at $t = t_3$ due to the competition between different growth directions. On the inboard side of the casting, a quite different situation is observed. Under simple thermal constraint, the undercooling in the platform is only that necessary to drive the motion of the dendrite tips. The front is free to follow the isotherms and is never constrained geometrically, as it is on side-A. Operating under thermal constraint only, the dendritic branching pattern, shown in Fig. 9b, is well ordered, in contrast to that shown in Fig. 9a. The other important geometrical feature to examine is the relationship between the angle of the platform in the y-z plane and the isotherm angle. If the curvature of the liquidus isotherm is relatively high, the dendritic front first reaches the platform at the corners of the casting. The spreading of the dendritic front into the platform, thus, proceeds from the

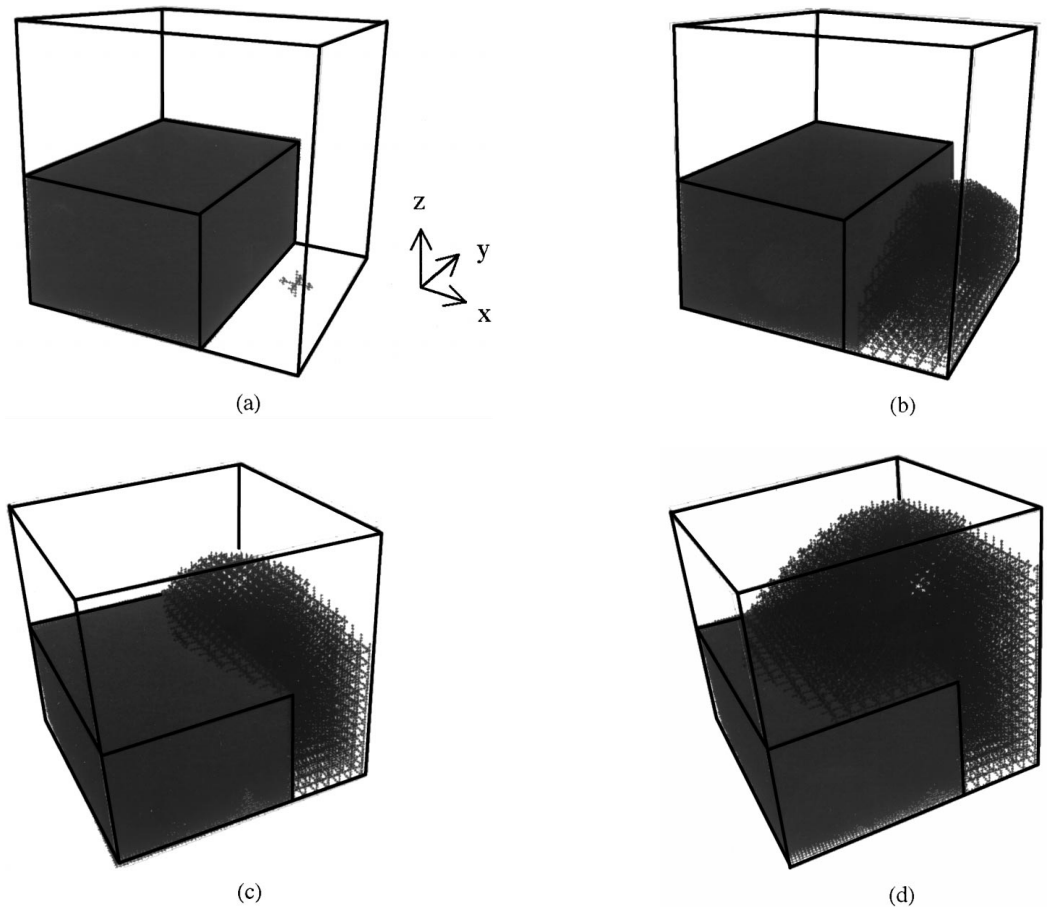

Figure 17 A three-dimensional view of the simulation sequence showing growth around a simple mold corner. The cubic domain has an edge length of 10 mm. $V = 0.2$ mm/s, $G_z = 1.5$ K/mm, $G_x = G_y = 0$.

outside toward the centerline. This accounts for the lateral growth patterns observed on the surface of the inboard side of the casting, in Fig. 8. For a front with less curvature, the spreading will proceed from the centerline outward, and the primary dendrites will be aligned along the z axis.

5. Convergence-fault model

While the separate consideration of the geometric effects discussed above may provide a qualitative understanding of the formation of various microstructural features, a quantitative description necessitates a more rigorous analysis of the interaction between these effects. To address this problem, a dendritic growth model was developed to predict the structures of the dendritic network resulting from the competitive growth which occurs in a dendritic array as the array adjusts to cross-sectional changes. By modeling the growth of the solid as a series of branching events, the dendritic structure is simulated and several effects of mold geometry and thermal conditions are reproduced. The convergence-fault defect structure is then predicted through analysis of the simulated dendritic structure.

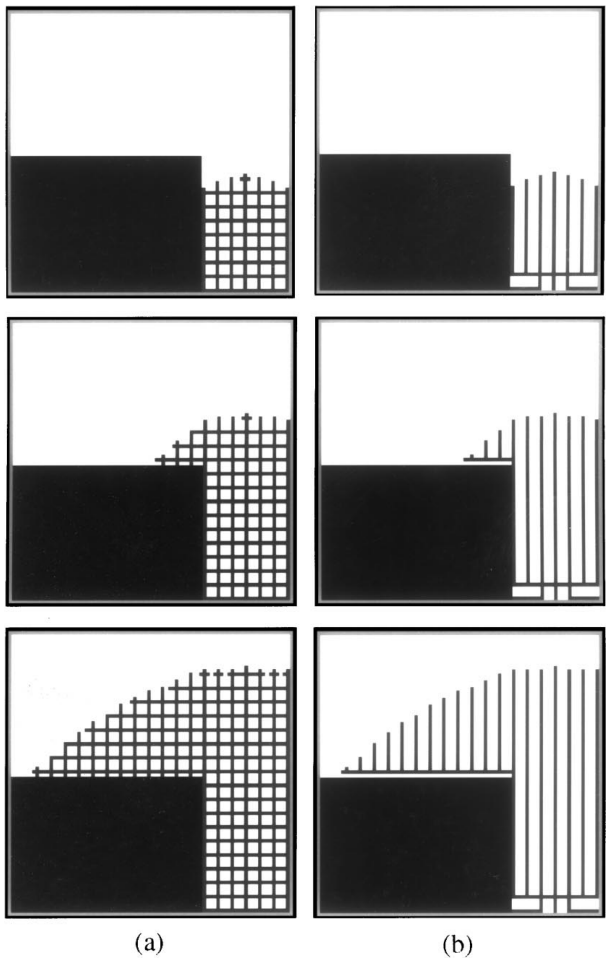

Figure 18 Two dimensional views of the $y = 0.5$ plane for the growth sequence shown in Fig. 17, showing the internal branch structure and the predicted shape of the dendritic solid as it propagates around the mold corner. The temperature gradient is 1.5 K/mm in the z direction, and the isotherm velocity is 0.2 mm/s. (a) Unfiltered: all branches shown, (b) Filtered: only branches with a length greater than λ are shown.

The dendritic crystal is modeled as a network of ⟨001⟩ needles. The tip of each needle is assumed to behave as a primary dendrite tip and is permitted to grow independently, along its axis. The tip velocity dependence

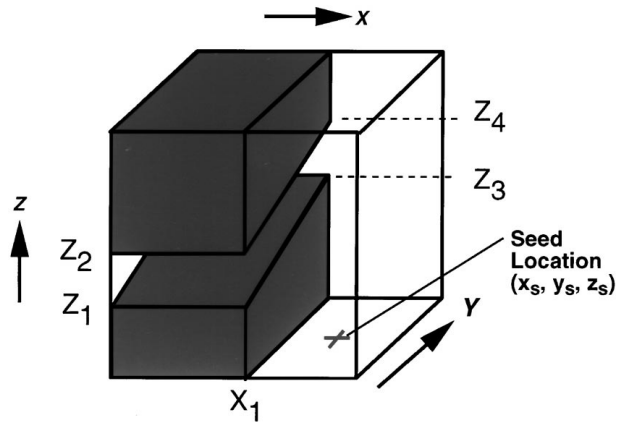

Figure 19 A schematic representation of the platform geometry used for the simulations.

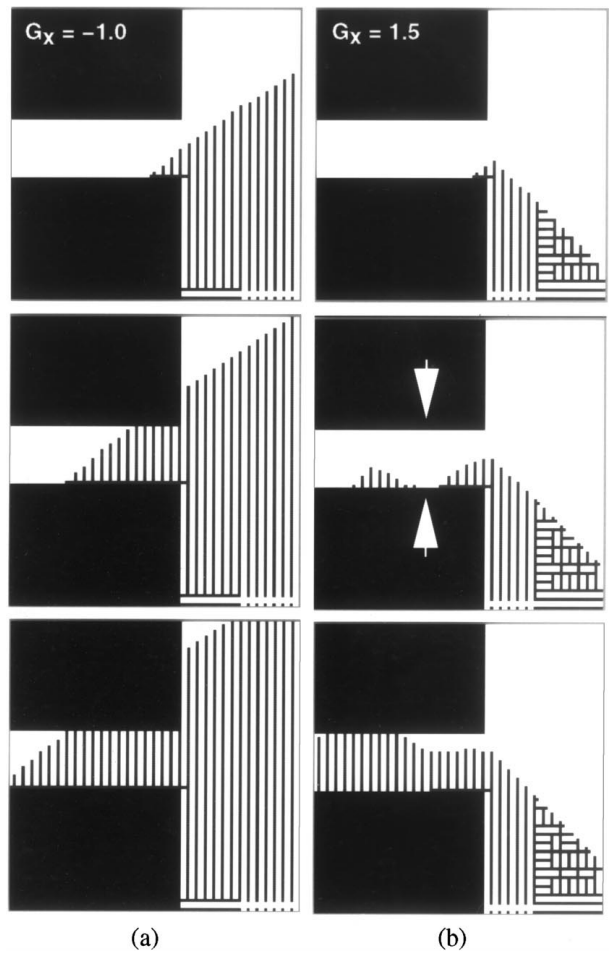

Figure 20 Time-sequences showing the simulated primary dendrite structure, illustrating the effect of the x component of the thermal gradient. The platform slope is 11.3 degrees, and the seed is located at (0.8, 0.5, 0). $G_z = 1.5$, $G_y = 0$, and the isotherm velocity is 0.2 mm/s. (a) For $G_x < 0$, the dendrite tips are not constrained by the mold geometry and are free to grow at their self-consistent temperature, resulting in a well-ordered structure, (b) For $G_x > 0$, significant undercooling develops due to the geometric constraint imposed by the mold. The corresponding dendritic structure exhibits convergent growth within the platform, at the indicated location.

on local undercooling is assumed to be well described by a power-law approximation, $V = A(\Delta T)^n$, of the tip velocity solution given by the analysis of Kurz *et al.* [10, 11]. For all simulations presented here, $A = 1.4 \times 10^{-5}$ m/sK^2 and $n = 2$ [12]. The possible growth directions for the needles are limited to the three $\langle 001 \rangle$ directions and their negatives. When a given branch reaches a specified length, λ, four branches are generated with growth directions along the four $\langle 001 \rangle$ axes orthogonal to the parent branch. Each new branch is then free to grow and branch independently according to its local temperature. Specification of the cube directions and a branch spacing is equivalent to constraining the network to grow on a cubic lattice, where the lattice vectors are [00λ], [0λ0], and [λ00]. To apply the model to a particular casting geometry, the lattice must be superimposed over the internal volume of the mold and a seed location must be specified. Once one or more seed needles are placed on the lattice, the solid is grown in a thermal field derived from thermal simulation results or specified as a particular temperature function, $T(x, y, z, t)$.

To illustrate the model, we now consider the simulation results shown in Fig. 17, for a dendritic front growing around a simple 90° mold corner, with a fixed thermal gradient. This 3-D sequence provides a picture of the overall shape of the growth front but does not permit analysis of the local primary direction. To obtain more specific information, we examine a 2-D section of the simulation domain, as shown in Fig. 18a. The

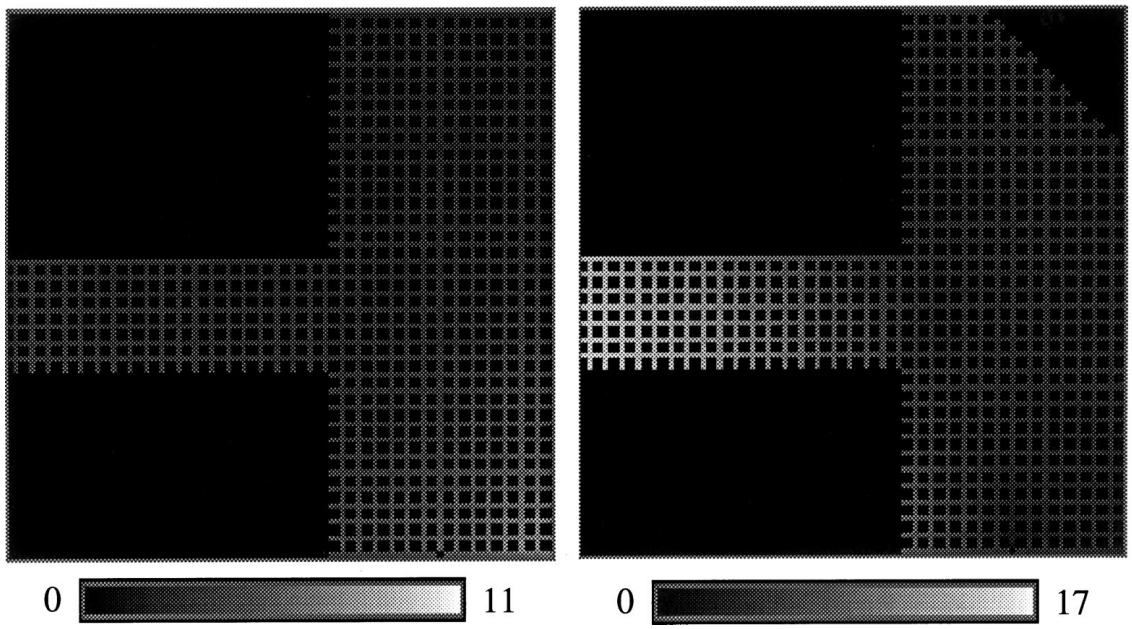

Figure 21 Two-dimensional views of the $y = 0.5$ plane showing the effect of G_x on the tip undercooling in the platform region for the simulation shown in Fig. 20. The shading scale gives undercooling (K).

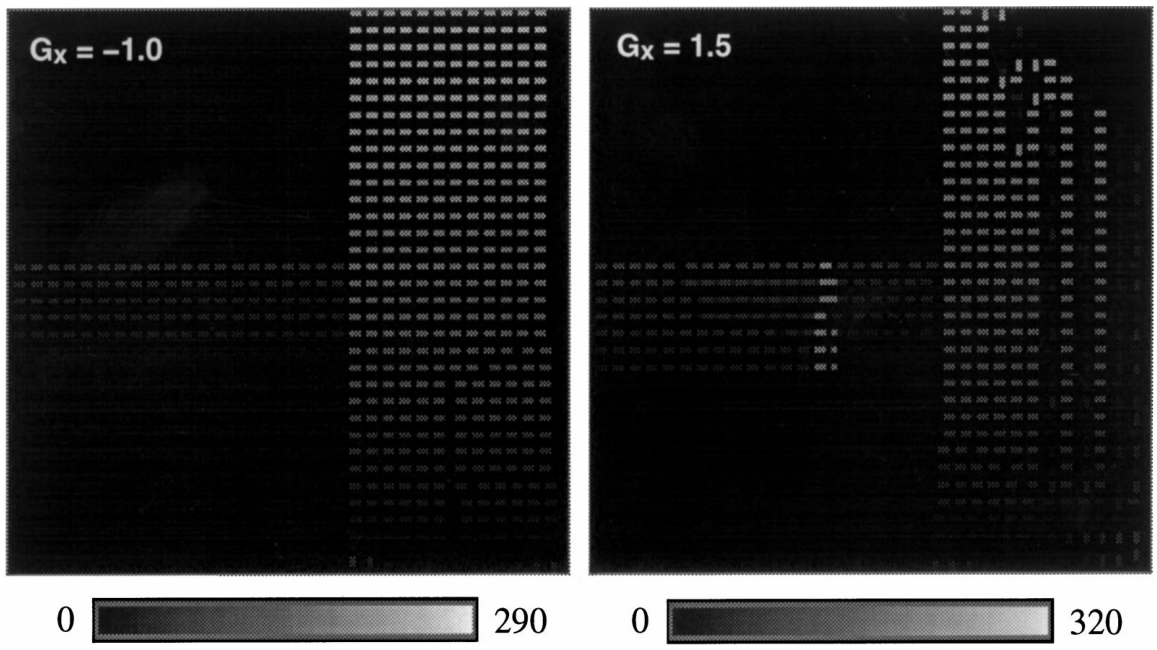

Figure 22 Plots of the connectivity parameter from the simulations shown in Fig. 20, indicating a vertical convergence-fault in the platform when $G_x > 0$.

local primary direction is revealed by eliminating from the display any branch which has been growing for any distance less than λ, Fig. 18b. The relatively simple geometry used for this simulation results in a dendritic structure which grows outward with a convex front at all points.

A more interesting shape of the dendritic front will result from a slightly more complex geometry as shown in Fig. 19. The platform geometry is specified by the five quantities $\{x_1, z_1, z_2, z_3, z_4\}$, all normalized by the cube edge dimension, which is 10 mm for all simulations to follow, unless otherwise noted. The crystallographic directions are along the coordinate axes, and the seed is a single needle originating on and growing normal to the plane $z = 0$. The location of the seed on this plane is specified by x_s and y_s. For this illustration, the isotherms are assumed to be planar and to move with constant velocity, with the gradient having components G_x, G_y, and G_z. To relate the predicted structure to the formation of convergence-faults, we introduce a parameter for the connectivity of the dendritic network. Here, we do not attempt to model the various forces which may lead to dendrite misorientation. Instead, we assume that when two branches collide, the probability that they will have developed some relative misorientation is proportional to the sum of the lengths that must

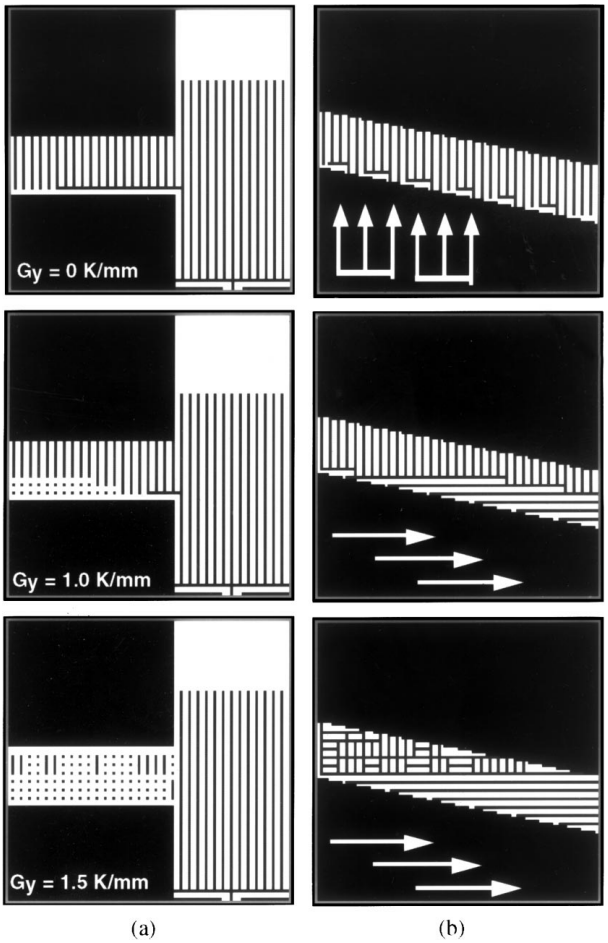

Figure 23 Two-dimensional views of the simulated structure showing the effect of the *y* component of the temperature gradient on the primary structure in the platform. $G_x = 0$, $G_z = 1.5$ K/mm, $V = 0.2$ mm/s, and the geometry is identical to that shown in Fig. 20. The views shown are for the (a) $y = 0.5$ and (b) $x = 0.2$ planes.

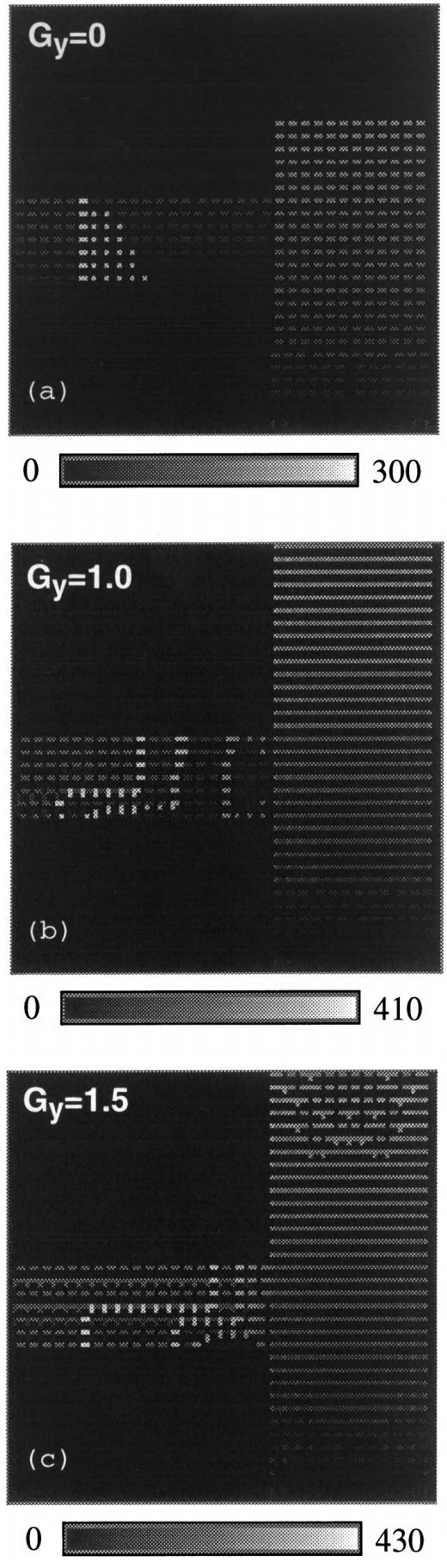

Figure 24 Plots of the connectivity parameter in the platform region for the simulations shown in Fig. 23, including another intermediate value of G_y. The indicated boundary changes from a vertical one to an L-shaped one as G_y increases to a point where the isotherm slope is greater than the platform slope, allowing the solid to first enter the platform at its highest point. This transition occurs between (a) and (b).

be traced backward from the two colliding tips along each of their respective growth histories to find a common point. Whenever a branch collides with another, this connectivity parameter is computed and plotted at

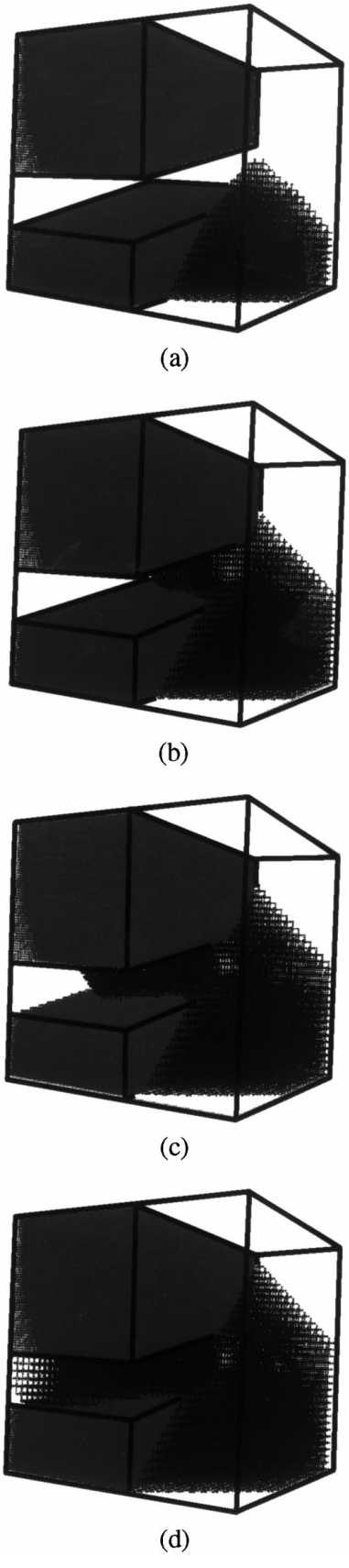

Figure 25 A three-dimensional growth sequence for $G_x = G_y = G_z =$ 1.5 K/mm and $V = 0.2$ mm/s. The geometry is identical to that in Fig. 20.

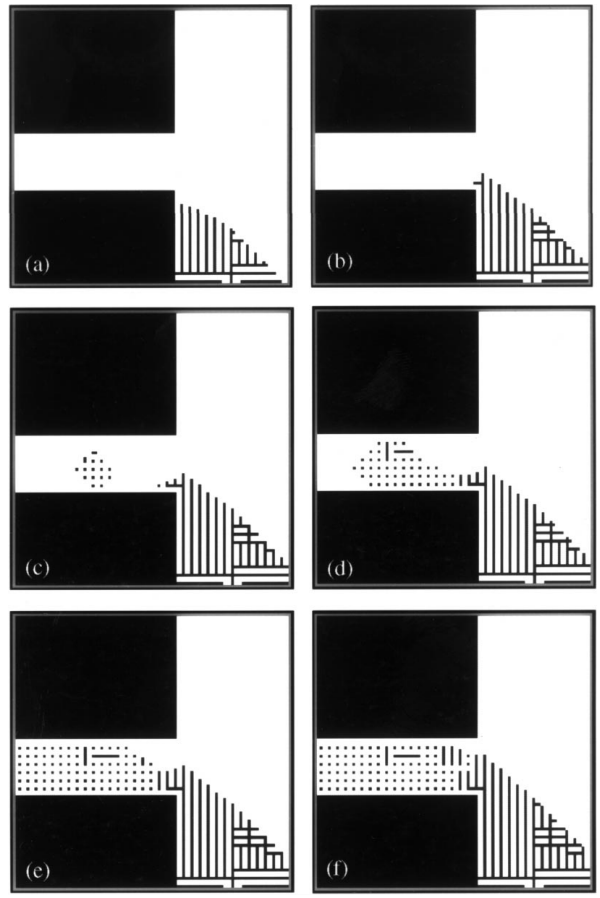

Figure 26 A time-sequence of the simulation shown in Fig. 25, revealing the convergent growth patterns on the $y = 0.5$ plane. Before growth can progress across the platform in the negative x direction, the front is intercepted by solid which is emerging from regions of the platform which are further toward the back ($y > 0.5$). The dots in the platform region, thus, represent growth in the direction normal to the viewing plane. (a) $t = 48$ s, (b) $t = 64$ s, (c) $t = 67$ s, (d) $t = 70$ s, (e) $t = 75$ s, (f) $t = 80$ s.

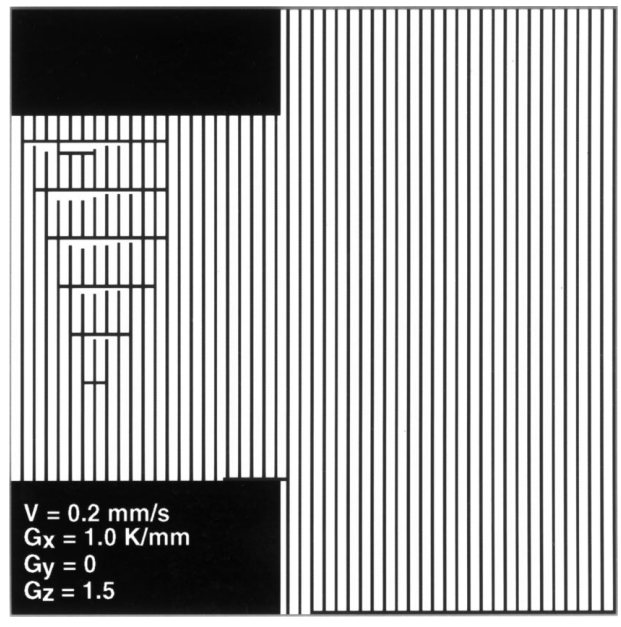

Figure 27 A two-dimensional view of the primary structure within a simulated platform with the dimensions and general thermal conditions of the side-A platform of casting T. The structure reveals convergent growth in this region as observed experimentally and shown in Fig. 9.

the location of impingement. In addition to the primary structure and connectivity, maps of tip undercooling can be generated.

The effect of the x component of the gradient, G_x, is shown in Fig. 20. The two-dimensional sections for two time sequences are shown. These are both taken at $y = 0.5$. In Fig. 20a, the temperature gradient points toward the platform side of the casting. In this case, geometric constraint is minimal, and the envelope containing the primary dendrite tips maintains a shape roughly equal to that of the isotherms. This situation permits very orderly solidification of the platform region with a consistent primary direction. In Fig. 20b, the gradient vector points away from the platform side of the casting. In this configuration, geometric constraint is significant and considerable liquid undercooling develops in the platform before the dendritic structure can grow around the corner. A grayscale map of tip undercooling from this example is given in Fig. 21, showing that this geometric constraint can result in very high undercooling in the platform. Growth in the platform region is, therefore, very fast. Since the platform is at an angle to the $z = 0$ plane, the solid first enters the platform at its lowest location, along the front face of the domain. Once the solid enters the platform at this forward location, growth is very rapid and the crystal spreads up the platform toward the rear of the domain. This explains the observation of the solid region which emerges in the center of the platform in Fig. 20b. That is, it is an indication of growth up the platform from

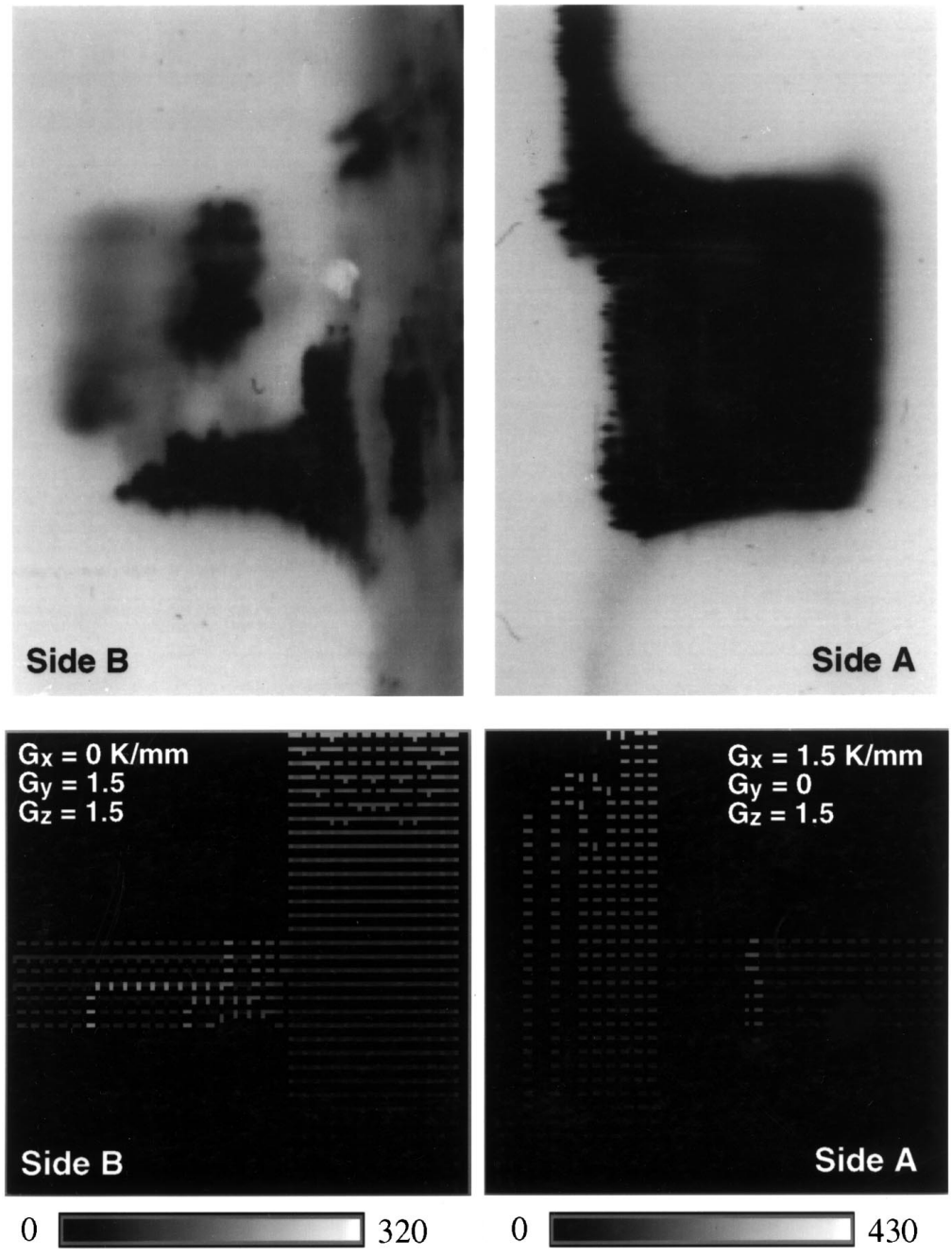

Figure 28 A plot of the boundaries indicated by the connectivity parameter compared with x-ray topographs showing observed low-angle boundaries in the platform. For $G_x < 0$ and G_y great enough for the isotherm slope to be greater than the platform slope (side-B), growth down the platform results in the characteristic L-shaped boundary, which is reproduced by the model. For a lower value of G_y and $G_x > 0$ (side-A), a vertical boundary is observed in experiment and, once again, is reproduced by the model.

front to back in the domain. With this type of growth sequence, there must be some location along the platform where the front to back growing region converges with the interface advancing across the platform. The convergence between these disjointed regions is predicted by the connectivity parameter, plotted in Fig. 22, which shows that a convergence-fault is indicated for the conditions simulated in Fig. 20b but not for those in Fig. 20a. In these plots, the value of the connectivity parameter gradually increases in the z direction, even for a perfect array of primary dendrites exhibiting no convergent growth patterns. This is expected since two adjacent primaries will continually generate secondaries which impinge upon each other. Since the shortest connecting circuit always includes the parent branch for the two primaries, the connectivity parameter will continue to increase. Such gradual increases in the connectivity parameter are, thus, not indications of convergence-faults. Instead, convergence-faults are indicated by discontinuities in the connectivity parameter, as in Fig. 22b.

The effect of G_y on the dendritic structure is shown in the 2-D views of the $y = 0.5$ plane in Fig. 23. In the first two plots, G_y is low enough to allow the front to first penetrate the platform on the front surface, which is its lowest point. In the latter two plots, G_y is higher and the solid enters the platform along the back surface, which is its highest point. Subsequent growth is down the platform, towards the front of the casting. The associated plots in Fig. 24 show that the two possible growth patterns result in two different types of connectivity boundaries. When the solid enters the platform at the lowest point, the boundary is generally vertical. When the solid enters the platform at the highest point and grows downward, an L-shaped boundary is observed and the magnitude of the connectivity parameter is much higher.

We now consider a combination of the two simple cases above. For the same geometry, a temperature gradient vector in the [111] direction is specified. Fig. 25 shows the resulting 3-D growth sequence. Once again, the geometric constraint allows high liquid undercooling to develop in the platform. In this case, however, the solid first penetrates the platform at the back of the domain, at its highest location. Growth out into the platform and down toward the front occurs rapidly. The two solid fronts then "zip" together along the edge of the platform. A two-dimensional view of the same simulation is shown in Fig. 26, for $y = 0.5$. Here, the solid in the platform emerges from the rear and converges with the part of the front which is advancing across the platform. In this case, the boundary is clearly indicated by an obvious change in local primary direction, where the dots represent growth normal to the viewing plane.

To summarize the capabilities of the tip-growth convergence-fault model, we examine three examples where the model has reproduced features observed in the test castings. The first example, shown in Fig. 23, is the prediction of lateral growth in the side-B platform of specimen T. This prediction is consistent with the microstructure shown in Fig. 8, revealing that primary growth direction on the surface of the side-B platform was, indeed, the y direction. The model also predicts some of the features observed in the interior of the platform, shown in Fig. 9a. The actual platform geometry and branch spacing from casting A were used to generate the simulated structure shown in Fig. 27. Finally, Fig. 28 shows that the two types of boundaries observed in the platform of the test castings are qualitatively reproduced by the model. When $G_x \leq 0$ and G_y is great enough so that the isotherm slope in the in the y-z plane is greater than the platform slope, L-shaped boundaries are produced by the model. When $G_x > 0$, a planar boundary is produced. This is in agreement with experimental observation, as shown by the x-ray topographs, also shown in Fig. 28.

6. Conclusions

The low-angle boundary structure in a single-crystal casting is directly related to the shape of the dendritic envelope as it spreads through the mold. As the front advances, primary dendrites may experience slight deviations in orientation which may or may not lead to a low-angle boundary in the final casting. When the dendritic front moves as a continuous smooth envelope, these deviations can be accommodated gradually and may not result in a detectable boundary in the final casting. If the front becomes disjointed, however, then different parts of the front may respond to local conditions independently, allowing the possibility that large relative misorientations may develop. If the different regions are permitted to rejoin, the accumulated misorientation will result in a low-angle boundary at the surface of convergence. This convergence-fault mechanism is likely to operate where geometric constraint dictates the shape of the growth front. This is most important near mold corners as well as near the emergence point of the seed or grain selector, where many low-angle boundaries are observed. Based on the geometric sensitivity of this mechanism, casting designers must carefully consider the response of the growing dendritic solid to the geometry of the mold and the thermal conditions, if these convergence-faults are to be avoided.

The tip-growth lattice model presented here is one technique for evaluating the primary structure which will evolve in a casting of a given geometry for a given set of thermal conditions. With this technique, local primary direction can be identified, a map of tip undercooling can be generated, and convergent growth patterns can be predicted.

The severity of the convergent growth can then be determined using a connectivity parameter which provides an indication of the likelihood for the formation of a convergence-fault in a particular location. Admittedly, this connectivity parameter is an oversimplified descriptor of the dendritic array and only a first order indicator for convergence-fault location, since it addresses only the branching geometry of the array. A more complete parameter would include the cumulative effects of the thermal and flow fields relative to the local growth direction. Despite the simplicity of the connectivity parameter used, the model predicted several of the

defect structures observed in the single-crystal castings, indicating that the branching geometry of the dendritic array, as described by the connectivity parameter, is a primary factor in convergence-fault formation.

Acknowledgements

The authors would like to thank B. A. Mueller (Howmet Corporation) for supplying the castings used for this study. Additional thanks go to D. R. Black and H. Burdette for X-ray topography, A. R. Roosen for the 3-D rendering of the growth model, and to L.C. Smith for metallographic specimen preparation. The authors would also like to acknowledge the National Synchrotron Light Source at the Brookhaven National Laboratory, where the X-ray topography was performed.

References

1. M. C. SCHNEIDER, J. P. GU, C. BECKERMANN, W. J. BOETTINGER and U. R. KATTNER, *Metall. Mater. Trans.* **A28** (1997) 1517.
2. E. V. AGAPOVA, G. N. PANKIN, V. V. PONOMAREV, V. N. LARIONOV and A. YA DENISOV, *Izv. Akad. Nauk SSSR, Metally* **2** (1989) 104.
3. U. PAUL, P. R. SAHM and D. GOLDSCHMIDT, *Mat. Sc. and Eng.* **A173** (1993) 49.
4. D. BELLET, P. BASTI, N. SIREDEY, J. LACAZE, A. GEORGE and J. P. MICHEL, in "Proc. EUROMAT '89 Conf.," edited by H. E. Exner and V. Schumacher (DGM Informationsgellschaft, 1990) p. 413.
5. N. SIREDEY, M. BOUFOUSSI, S. DENIS and J. LACAZE, *J. Crystal Growth* **130** (1993) 132.
6. M. RAPPAZ and E. BLANK, *ibid.* **74** (1986) 67.
7. R. J. SCHAEFER, D. R. BLACK, M. D. VAUDIN, B. R. MUELLER and A. F. GIAMEI, in "Solidification Processing 1997: Proc. 4th Decennial International Conference on Solidification Processing," edited by J. Beech and H. Jones (University of Sheffield,1997) p. 37.
8. J. P. GU, C. BECKERMANN and A. F. GIAMEI, *Metall. Mater. Trans.* **28A** (1997) 1533.
9. S. M. COPLEY, A. F. GIAMEI, S. M. JOHNSON and M. F. HORNBECKER, *Met. Trans.* **A1** (1970) 2193.
10. W. KURZ and D. J. FISHER, *Acta Metall.* **29** (1981) 11.
11. W. KURZ, B. GIOVANOLA and R. TRIVEDI, *ibid.* **34** (1986) 823.
12. TH. IMWINKELRIED, J.-L. DESBIOLLES, CH.-A. GANDIN, M. RAPPAZ, S. ROSSMAN and PH. THEVOC, in "Modeling of Casting, Welding, and Advanced Solidification Processes VI," edited by T. S. Piwonka, V. Voller and L. Katgerman (The Minerals, Metals and Materials Society, Warrendale, 1993).

Received 10 February
and accepted 22 July 1999